



# A Low Mach Number IMEX Flux Splitting for the Level Set Ghost Fluid Method

Jonas Zeifang<sup>1,2</sup> · Andrea Beck<sup>2,3</sup>

Received: 22 September 2020 / Revised: 6 April 2021 / Accepted: 14 April 2021  
© The Author(s) 2021

## Abstract

Considering droplet phenomena at low Mach numbers, large differences in the magnitude of the occurring characteristic waves are presented. As acoustic phenomena often play a minor role in such applications, classical explicit schemes which resolve these waves suffer from a very restrictive timestep restriction. In this work, a novel scheme based on a specific level set ghost fluid method and an implicit-explicit (IMEX) flux splitting is proposed to overcome this timestep restriction. A fully implicit narrow band around the sharp phase interface is combined with a splitting of the convective and acoustic phenomena away from the interface. In this part of the domain, the IMEX Runge-Kutta time discretization and the high order discontinuous Galerkin spectral element method are applied to achieve high accuracies in the bulk phases. It is shown that for low Mach numbers a significant gain in computational time can be achieved compared to a fully explicit method. Applications to typical droplet dynamic phenomena validate the proposed method and illustrate its capabilities.

**Keywords** IMEX flux splitting · Level set method · Ghost fluid method · Low Mach number flows

**Mathematics Subject Classification** 65N30 · 65Z05 · 35Q35

---

✉ Jonas Zeifang  
jonas.zeifang@uhasselt.be  
Andrea Beck  
andrea.beck@ovgu.de

<sup>1</sup> Faculty of Sciences, Hasselt University, Agoralaan Gebouw D, BE-3590 Diepenbeek, Belgium

<sup>2</sup> Institute of Aerodynamics and Gas Dynamics, University of Stuttgart, Pfaffenwaldring 21, 70569 Stuttgart, Germany

<sup>3</sup> Laboratory of Fluid Dynamics and Technical Flows, Otto von Guericke University Magdeburg, Universitätsplatz 2, 39106 Magdeburg, Germany

## 1 Introduction

In many situations in nature or technical applications, more than one material phase is present. Often, two phases are separated by a distinct interface as it is the case for, e.g., rain drops or spray related processes. In such applications, the characteristic Mach number  $Ma = \frac{\|\mathbf{u}\|_2}{c}$ , relating the velocity of the convective phenomena  $\mathbf{u}$  to the speed of sound  $c$ , often covers a wide range of values. Especially in the liquid phase, the Mach numbers are often low, whereas in the gaseous phase higher Mach numbers are present. The simulation of such phenomena requires numerical methods which are capable of treating flows with a wide range of Mach numbers accurately (including the correct asymptotic scaling) and efficiency. Considering the characteristics of the Euler equations shows the difficulties numerical methods are facing. For large Mach numbers ( $Ma = \mathcal{O}(1)$ ) the Euler equations are hyperbolic. In the limit ( $Ma \rightarrow 0$ ) they change their type to hyperbolic-elliptic. For small Mach numbers ( $Ma \ll 1$ ), the speeds of the present characteristic waves differ tremendously: the acoustic waves are much faster than the convective phenomena. If acoustics plays a minor role, standard explicit methods are not efficient as they have to resolve the fast characteristic waves for stability reasons, leading to a prohibitively small timestep.

To overcome this timestep restriction, different approaches exist, mostly relying on the implicit time discretization: fully implicit time discretization for the modeling of two-phase flow are, e.g., proposed in [25, 31, 47]. Another class of schemes are pressure-based methods, relying on the implicit solution of an elliptic equation for the pressure. They can be seen as an extension of incompressible schemes and require a reformulation of the equation of state (EOS), which is a non-trivial task for complex EOS. Pressure-based methods have been derived for multiphase flows, e.g., in [4, 15, 18, 26, 35, 45]. Another option are implicit-explicit (IMEX) flux splitting schemes which are based on the separation of the fast acoustic and slow convective waves of the flux. The idea is to treat the fast waves implicitly, while the slow waves are treated explicitly. This splitting often serves as a starting point for the derivation of pressure-based methods, see, e.g., [13, 30, 51, 64]. The application of flux splittings with general EOS is often straightforward as the EOS does not have to be reformulated. Nevertheless, IMEX schemes have only rarely been applied to multiphase problems, see [7, 8, 55].

Low Mach number two-phase flows not only necessitate a specific design to tackle the different orders of magnitude of the characteristic waves. Additionally, the presence of two phases demands a modeling of the different states of matter and their coupling. For the modeling of multiphase flows mainly two concepts exist: diffuse and sharp interface approaches. Common approaches to capture the interface in a sharp interface scheme are the volume-of-fluid [33] and the level set method [54, 62]. The level set method has the advantage that the normals and the curvature of the phase interface are directly given by the derivatives of the level set function and hence the interface geometry does not have to be reconstructed, as it would be the case for the volume-of-fluid method. For the modeling of the physical phenomena at the phase boundary, the ghost fluid method (GFM) has been introduced in [23]. In this work, we focus on a specific type of a sharp interface GFM based on the ideas of [49]. Here, a multiphase Riemann problem is solved at the phase boundaries. The idea has been adapted in [20, 21] and slightly modified in [37, 50]. A discontinuous Galerkin scheme [32] is used for the spatial discretization of the bulk phases and at the phase boundary a finite volume sub-cell refinement [60] is applied. This framework will serve as a foundation of this work.

Since IMEX flux splitting schemes have been found to be well suited for low Mach number computations within a discontinuous Galerkin framework [72, 73], the idea in this work is to combine an IMEX flux splitting scheme with the sharp interface level set ghost fluid method (LSGFM). Although the fully implicit time discretization has been used within the LSGFM [31, 37, 47], IMEX flux splitting schemes have not been investigated in this context. As a flux splitting, the idea of Toro and Vázquez-Cendón (TV) [67] and its extension to general EOS [66] are used. Hence, the main novelty of this paper is the analysis and presentation of how an IMEX flux splitting can be combined with a discontinuous Galerkin sharp interface LSGFM to overcome the restrictive timestep restriction of weakly compressible multiphase flows.

We will proceed as follows. In Sect. 2, the considered governing equations are summarized. Following in Sect. 3, the IMEX LSGFM is described. Starting with a short summary on the level set ghost fluid framework in Sect. 3.1, it is described how IMEX flux splitting schemes can be applied in Sect. 3.2. Next, novel scheme is validated and its efficiency is investigated in Sect. 4. Following, some illustrative applications are shown in Sect. 5. Finally, in Sect. 6 conclusion and outlook are given.

## 2 Governing Equations

The idea of the sharp interface approach is to model two-phase flows as two pure bulk phases without a mixing zone. Inside the pure phases, the Euler equations are chosen to model the physical behavior of the fluids. In three dimensions they are given by

$$\partial_t \mathbf{w} + \nabla_x \cdot \mathbf{F}(\mathbf{w}) = 0 \quad \text{with} \quad \mathbf{w} := \begin{pmatrix} \rho \\ \rho \mathbf{u} \\ E \end{pmatrix}$$

$$\text{and} \quad \mathbf{F}(\mathbf{w}) := \begin{pmatrix} \rho \mathbf{u} \\ \rho \mathbf{u} \otimes \mathbf{u} + p \cdot \mathbf{Id} \\ \mathbf{u}(E + p) \end{pmatrix}, \tag{1}$$

with density  $\rho$ , velocity  $\mathbf{u} = (u, v, w)^T$ , total energy  $E$ , pressure  $p$  and the three dimensional identity matrix  $\mathbf{Id}$ . The primitive state vector is given as  $\mathbf{w}_{\text{prim}} = (\rho, \mathbf{u}, p)^T$ . The pressure is linked to the density and the specific internal energy  $\epsilon := \frac{E}{\rho} - \frac{\|\mathbf{u}\|_2^2}{2}$  via an EOS. For gases, the ideal gas EOS

$$p(\rho, \epsilon) = (\gamma - 1)\rho\epsilon$$

with the isentropic coefficient  $\gamma$  is chosen. Liquids are modeled with the stiffened gas EOS:

$$p(\rho, \epsilon) = (\gamma - 1)\rho\epsilon - \gamma p_\infty,$$

where the material-dependent parameter  $p_\infty$  is used to model the increased stiffness of liquids compared to gases. Note that the algorithm introduced in this work is not restricted to the use of such simple EOS. It is also possible to use more complex or tabulated EOS [24].

The phase interface separating the two phases is tracked by a level set function  $\Phi$ , describing the signed distance to the phase interface. Hence its root describes the position of the phase interface. The level set function is transported with a velocity field  $\mathbf{s}$  according to

$$\partial_t \Phi + \mathbf{s} \cdot \nabla_x \Phi = 0. \tag{2}$$

The geometrical quantities of the phase interface, i.e., the normal vector  $\mathbf{n}_\Phi$  and the curvature  $\kappa_\Phi$ , are directly given by the derivatives of the level set field [17].

### 3 IMEX Flux Splitting for the LSGFM

In this section, first the compressible LSGFM according to [21, 37, 50] is briefly recalled. Following, it is outlined how IMEX flux splitting schemes can be used to enable efficient simulations at low Mach numbers.

#### 3.1 The LSGFM

##### 3.1.1 Domain Decomposition

The position of the phase interface is described by the zero position of the level set function. Hence, the sign of the level set field can be used as an identifier to divide the computational domain  $\Omega$  into a liquid  $\Omega^l$  and a gaseous domain  $\Omega^g$ . Discretely, the interface position is shifted to the next boundary of the discretization elements, in the following called the surrogate surface. To obtain an accurate scheme, the high order discontinuous Galerkin spectral element method (DGSEM) [32, 41] is applied for the spatial discretization. The DGSEM is based on the polynomial approximation of the solution as a tensor-product of nodal one-dimensional Lagrange polynomials of degree  $N$  inside each element  $C$  of the computational mesh  $C \in \Omega$ . For this piecewise smooth function  $\mathbf{w}_h$  the weak formulation is then given by

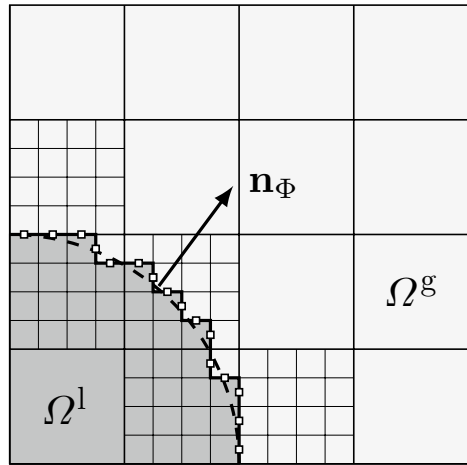
$$\frac{\partial}{\partial t} \int_C \mathbf{w}_h \phi(\mathbf{x}) d\mathbf{x} + \oint_{\partial C} \mathbf{f}_n^* \phi(\mathbf{x}) ds - \int_C \mathbf{F}(\mathbf{w}_h) \cdot \nabla \phi(\mathbf{x}) d\mathbf{x} = 0, \tag{3}$$

for every polynomial test function  $\phi(\mathbf{x})$  of degree  $N$ . Across the element boundaries discontinuities are allowed and the elements are coupled via a numerical flux function  $\mathbf{f}^*$ . Choosing the same nodal Lagrange polynomials of degree  $N$  as test functions and ansatz functions, leads to the DGSEM which is  $(N + 1)$ th-order accurate in space. A detailed description of the used DGSEM can be found in [32] and an overview on the actual implementation is provided in [42]. The core method is available as open source software FLEXI<sup>1</sup>.

Due to its solution representation, each grid element contains multiple (nodal) degrees of freedom (DOFs). In the LSGFM context this leads to a poor relation of discrete interface resolution per DOF. Therefore, a refinement of the elements adjacent to the phase interface is applied. For that purpose, the mixed finite volume (FV)/DG formulation from [60, 61] is used. Figure 1 illustrates this sub-cell refinement in the cells neighboring the phase interface and the domain decomposition in a liquid and a gaseous domain  $\Omega^l$  and  $\Omega^g$ , respectively which are separated by the surrogate surface  $\Gamma$ .

<sup>1</sup> www.flexi-project.org, GNU GPL v3.0

**Fig. 1** Schematic view of domain decomposition with the compressible LSGFM into a liquid (dark gray) and a gaseous domain (light gray). Large squares denote the elements of the DG grid, while small squares denote the elements of the refined FV sub-cell grid. The zero isocontour of the level set with its normal vector  $\mathbf{n}_\Phi$  is indicated with a dashed line and positions on the surrogate surface, where a two-phase Riemann problem is solved are marked with a small white square



### 3.1.2 Interface Treatment

*Two-phase Riemann solver* While in the pure bulk phases, no multiphase effects have to be considered, directly at the discrete phase interface a special treatment of the fluxes is necessary. The procedure at the phase boundary is based on the idea outlined in [49], to use the solution of a two-phase Riemann problem as a boundary condition for the pure phases. This approach has been modified in [20, 21] to use the approximate solution of the two-phase Riemann problem instead of the exact solution. In Fig. 1, positions on the surrogate surface, where two-phase Riemann problems are solved are marked with a small white square.

In this work, the HLLP Riemann solver from [20, 59] is used at the phase boundary. This Riemann solver is based on the well-known HLLC Riemann solver, where the contact discontinuity “C” is considered as the phase boundary “P”. It enables the treatment of surface tension effects by considering the pressure jump of the Young-Laplace law in the jump conditions of the Riemann solver. From the solution of the HLLP Riemann solver three quantities can be extracted: fluxes for the liquid and the gaseous phase  $f_1^*$ ,  $f_g^*$ , the velocity of the phase interface  $s^\#$  and so-called ghost states for the liquid and the gaseous phase. For a liquid cell adjacent to the interface, its ghost state is a gaseous state and vice versa. Here, the ghost states are chosen as the interchanged initial conditions of the two-phase Riemann problem. They are used if the interface position moves and a sub-cell changes its assignment to the liquid or gaseous domain.

Note that the GFM is inherently non-conservative [23, 49]. This stems from the non-equality of the fluxes at the interface  $f_g^* \neq f_1^*$  and from the definition of the new states if a sub-cell element changes its assignment from the liquid to the gaseous domain or vice versa. Attempts to overcome the non-conservativity of the GFM for incompressible flows relying the divergence-free condition of the incompressible velocity field have been made in, e.g., [16, 52, 53]. For compressible flows, an attempt to improve the conservativity has been presented in [46]. The idea in [46] is to modify the novel states which are set when the interface moves. Nevertheless, it is not considered here as this modification can have an unfavorable influence on the stability.

*Velocity extrapolation* From the solution of the two-phase Riemann problem, the velocity at the phase boundary  $s^\#$  can be extracted. This pointwise available information is then used to construct a velocity field  $\mathbf{s}$  for the transport of the level set field. This is done by solving a Hamilton-Jacobi-type equation [56]

$$\partial_\tau s^m + H_{\text{extvel}}(\nabla_x s^m) = 0, \quad \text{for the directions } m = 1, 2, 3$$

with the numerical Hamiltonian

$$\begin{aligned} H_{\text{extvel}}(\nabla_x s^m) &\approx H_{\text{extvel}}^{\text{LF}}(\nabla_x^+ s^m, \nabla_x^- s^m) \\ &:= \frac{1}{2}(\text{sgn}(\Phi)(\mathbf{n}_\Phi \cdot (\nabla_x^+ s^m + \nabla_x^- s^m)) - |\mathbf{n}_\Phi| \cdot (\nabla_x^+ s^m - \nabla_x^- s^m)), \end{aligned}$$

according to [19], with the componentwise absolute value of the level set normal  $|\mathbf{n}_\Phi|$  and a numerical sign function  $\text{sgn}$ . The discretization of the up- and downwind gradients  $\nabla_x^+$  and  $\nabla_x^-$  is done with the HJ-WENO scheme from [36] and the pseudo time iteration is performed with a 3rd order explicit Runge-Kutta method. More details on this can be found in [19].

*Level set transport:* The resulting velocity field is then used for the solution of Eq. (2). Differently to the weak form of Eq. (1) given in Eq. (3), the variational form for the level set transport reads

$$\frac{\partial}{\partial t} \int_C \Phi_h \phi(x) dx + \int_{\partial C} (\mathbf{s} \cdot \nabla \Phi_h) \phi(x) ds + \int_{C \setminus \partial C} (\mathbf{s} \cdot \nabla \Phi_h) \phi(x) dx = 0.$$

As this is a non-conservative equation, the discretization has to be slightly adapted. Similarly to the mixed DGSEM/FV formulation used for the bulk phases, the solution  $\Phi_h$  is either represented with the tensor-product of nodal one-dimensional Lagrange polynomials of degree  $N$  (DGSEM) or with the piecewise constant refined FV representation. When choosing a path-conservative formulation for the discretization of the weak form introduces now modified numerical fluxes at the cell boundaries to account for the non-conservativity of the equation. Details on the derivation of this specific fluxes can be found in [37].

*Level set reinitialization* Unfortunately, the level set field does not retain its signed distance property during the advection and hence it has to be reinitialized. Again, a Hamilton-Jacobi equation

$$\partial_\tau \Phi + H_{\text{reinit}}(\nabla_x \Phi) = 0$$

is solved with the WENO scheme from [36] and an explicit 3rd order Runge-Kutta scheme. The Hamiltonian  $H_{\text{reinit}}(\nabla_x \Phi) = \text{sign}(\Phi)(|\nabla_x \Phi| - 1)$  is approximated with the numerical Hamiltonian according to [17] by

$$\begin{aligned} H_{\text{reinit}}(\nabla_x \Phi) &\approx H_{\text{reinit}}^{\text{God}}(\nabla_x^+ \Phi, \nabla_x^- \Phi) \\ &:= \text{sgn}(\Phi) \begin{cases} \sqrt{\max(a_1, b_1) + \max(a_2, b_2) + \max(a_3, b_3)} - 1, & \text{if } \text{sgn}(\Phi) \leq 0, \\ \sqrt{\max(c_1, d_1) + \max(c_2, d_2) + \max(c_3, d_3)} - 1, & \text{else,} \end{cases} \end{aligned}$$

where

$$\begin{aligned} a_i &:= \max(|(\nabla_x^+ \Phi)_i|^2, 0), & b_i &:= -\min(|(\nabla_x^- \Phi)_i|^2, 0), \\ c_i &:= -\min(|(\nabla_x^+ \Phi)_i|^2, 0), & d_i &:= \max(|(\nabla_x^- \Phi)_i|^2, 0). \end{aligned}$$

The reinitialization and the velocity extrapolation procedure are proceeded in pseudo time until information from the level set zero position has propagated two to three mesh elements away from the phase interface.

*Interface derivatives calculation* As stated before, the geometrical quantities of the phase interface, i.e., normal vector and interface curvature, are directly given by the derivatives of the level set field. It has been found to be beneficial to use second order finite differences for the calculation of the derivatives, although the level set field is discretized with higher order polynomials [48]. This approach is also pursued here, i.e., the gradients of the level set, required for the normals of the phase interface  $\mathbf{n}_\Phi = \nabla_x \Phi / |\nabla_x \Phi|$ , are discretely calculated at a DOF  $ijk$  with

$$\begin{aligned} \nabla_x \Phi_{ijk} &= (\Phi_{x_1}, \Phi_{x_2}, \Phi_{x_3})^T \\ &\approx \left( \frac{\Phi_{(i-1)jk} - \Phi_{(i+1)jk}}{2\Delta x_{ijk}}, \frac{\Phi_{i(j-1)k} - \Phi_{i(j+1)k}}{2\Delta x_{ijk}}, \frac{\Phi_{ij(k-1)} - \Phi_{ij(k+1)}}{2\Delta x_{ijk}} \right)^T, \end{aligned} \tag{4}$$

where  $\Phi_{x_1}$  denotes the derivative of the level set in  $x_1$ -direction. The level set normal vector is used to transform the states for the solution of the two-phase Riemann solver such that the Riemann problem is solved in the phase normal direction, i.e., in the normal direction of the physical phase interface. This ensures that the pressure jump introduced by the surface tension acts in correct direction. The pressure jump is calculated via Young-Laplace law using the curvature of the phase interface

$$\begin{aligned} \kappa_\Phi := & \frac{\Phi_{x_1}^2 \Phi_{x_2 x_2} - 2\Phi_{x_1} \Phi_{x_2} \Phi_{x_1 x_2} + \Phi_{x_2}^2 \Phi_{x_1 x_1}}{|\nabla_x \Phi|^3} \\ & + \frac{\Phi_{x_1}^2 \Phi_{x_3 x_3} - 2\Phi_{x_1} \Phi_{x_3} \Phi_{x_1 x_3} + \Phi_{x_3}^2 \Phi_{x_1 x_1}}{|\nabla_x \Phi|^3} \\ & + \frac{\Phi_{x_2}^2 \Phi_{x_3 x_3} - 2\Phi_{x_2} \Phi_{x_3} \Phi_{x_2 x_3} + \Phi_{x_3}^2 \Phi_{x_2 x_2}}{|\nabla_x \Phi|^3}, \end{aligned}$$

where  $\Phi_{x_1 x_2}$  denotes the derivative  $\frac{\partial^2 \Phi}{\partial x_1 \partial x_2}$  and is obtained by applying the finite difference operator in Eq. (4) twice.

These procedures now serve as building blocks for the construction of the IMEX LSGFM, which is introduced in the next subsection.

### 3.2 The IMEX LSGFM

The idea of IMEX flux splittings is to separate the fast (acoustic) and the slow (convective) waves. To obtain a timestep restriction independent of the fast waves, they are then treated implicitly and the slow waves are treated explicitly. Fast waves are presented in Eq. (1) but not in Eq. (2). Therefore, the level set transport is treated purely explicitly and only for the time discretization of the Euler equations and an IMEX flux splitting scheme is applied.

#### 3.2.1 Overview of the Algorithm

In Fig. 2, it is illustrated how the different building blocks can now be assembled to a consistent algorithm, where the level set transport is handled explicitly. In a first step fully

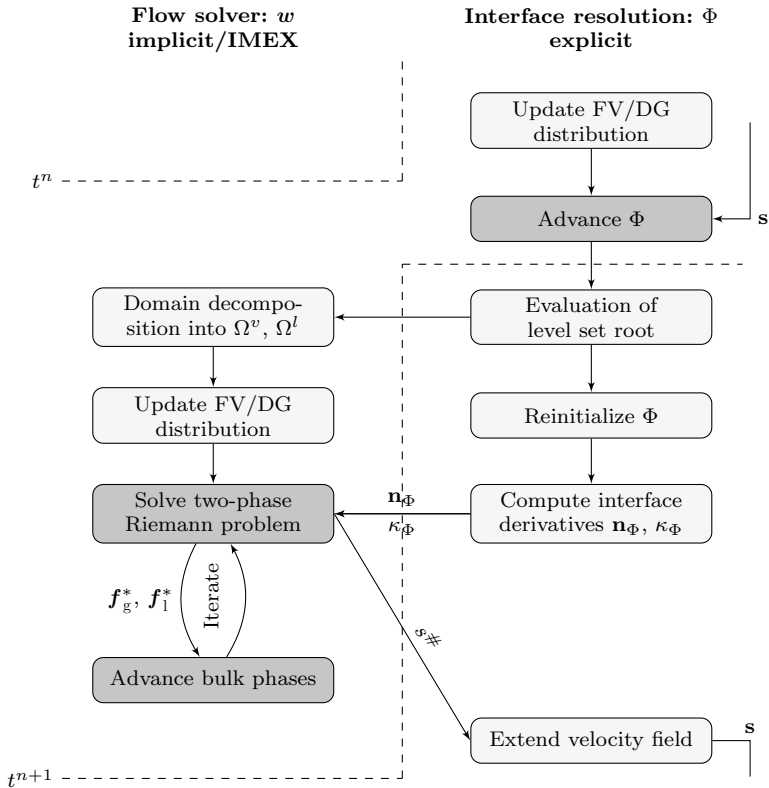


**Fig. 2** Schematic overview of IMEX LSGFM. Steps that are done in each Runge-Kutta stage are marked with dark gray, steps that are repeated only once per timestep are marked with light gray

implicit time discretization is applied to the flow field. The separation of the fast and slow waves using a flux splitting and leading to an IMEX discretization of the flow field is described thereafter.

- (i) Update the DG/FV distribution of the level set field according to the information about the position of the interface.
- (ii) Advance the level set field explicitly in time with the velocity field  $\mathbf{s}$  to obtain  $\Phi^{n+1}$  by solving Eq. (2).
- (iii) Define  $\Omega^l$  and  $\Omega^g$  at the new time instance  $t^{n+1}$  according to the sign of the level set field. Use the ghost states from the old time instance  $t^n$  if an assignment of a sub-cell has changed.
- (iv) Repeat step (i) for the flow solver.
- (v) Reinitialize the level set field to recover its signed distance property.
- (vi) Calculate the geometrical properties  $\mathbf{n}_\Phi^{n+1}$  and  $\kappa_\Phi^{n+1}$  of the phase interface at the new time instance.
- (vii) Iteratively advance the flow field using the implicit/IMEX time discretization.
  - Use the geometrical information  $\mathbf{n}_\Phi^{n+1}$  and  $\kappa_\Phi^{n+1}$  for the solution of the two-phase Riemann problems to obtain  $f_g^*, f_1^*, s^\#$  and the ghost states at the new time instance  $t^{n+1}$ .



- Use the fluxes from the HLLP solver  $f_g^*$  and  $f_1^*$  as boundary conditions for the bulk phases and advance the flow field (Eq. (1)).
- (viii) Construct the velocity field  $s$  for the level set transport from  $s^\#$ , when the iterative procedure from step (vii) has converged.
- (ix) Repeat steps (i)–(viii) until the final time  $t_{\text{end}}$  is reached.

This quasi-serial advancement of the level set function and the flow field ensures that the interface position of the initial guess for the implicit method is already at the correct location for  $t^{n+1}$ . Note that this coupling is first order in time. Nevertheless, the errors of the temporal discretization can be reduced by applying Runge-Kutta methods for the level set transport and the advancement of the flow field.

### 3.2.2 TV Flux Splitting

If a proper splitting of the Euler equations (1) is chosen and coupled with the above described algorithm, this allows timesteps being independent of the fast acoustic waves. There are a lot of options of how to split the flux of the Euler equations into an implicitly  $\tilde{F}(w)$  and explicitly treated flux  $\hat{F}(w)$  with  $F(w) = \tilde{F}(w) + \hat{F}(w)$ , see, e.g., [5, 12, 29, 67, 74]. In this work, the TV splitting approach according to [67] is used due to its simplicity and its ability to be applied to general EOS [66]. It splits the flux into a pressure system  $\tilde{F}(w)$  and an advection system  $\hat{F}(w)$  via

$$\tilde{F}(w) := \begin{pmatrix} 0 \\ p \cdot \mathbf{Id} \\ \mathbf{u}(\rho\epsilon + p) \end{pmatrix} \quad \text{and} \quad \hat{F}(w) := \begin{pmatrix} \rho\mathbf{u} \\ \rho\mathbf{u} \otimes \mathbf{u} \\ \frac{1}{2}\rho\mathbf{u}\|\mathbf{u}\|_2^2 \end{pmatrix}. \tag{5}$$

According to [66], the eigenvalues of the implicit subsystem are given by

$$\tilde{\lambda}_1 = \frac{1}{2}(\mathbf{u} \cdot \mathbf{n} - A), \quad \tilde{\lambda}_{2,3,4} = 0, \quad \tilde{\lambda}_5 = \frac{1}{2}(\mathbf{u} \cdot \mathbf{n} + A),$$

with

$$A := \sqrt{\|\mathbf{u}\|_2^2 + 4\left(\frac{\epsilon}{\rho} + \frac{p}{\rho^2}\right)\left(\frac{\partial\epsilon}{\partial p}\right)^{-1}}. \tag{6}$$

For the explicit subsystem the eigenvalues can be calculated as

$$\hat{\lambda}_1 = 0, \quad \hat{\lambda}_{2,3,4,5} = \mathbf{u} \cdot \mathbf{n}.$$

From this one can see, that only convective phenomena influence the timestep if only the advection system is treated explicitly as the timestep of the DGSEM is given by

$$\Delta t = \left( \frac{\text{CFL} \cdot l_{\text{ref}}}{|\hat{\lambda}|_{\max}(2N + 1)} \right)_{\min_{\Omega}}, \tag{7}$$

for a characteristic length scale  $l_{\text{ref}}$  of the discretization elements and  $\text{CFL} \lesssim 1$ . For the DGSEM, the CFL number is typically scaled with an empirically obtained constant which is specific for the chosen Runge-Kutta method and polynomial degree, see, e.g., [28]. In

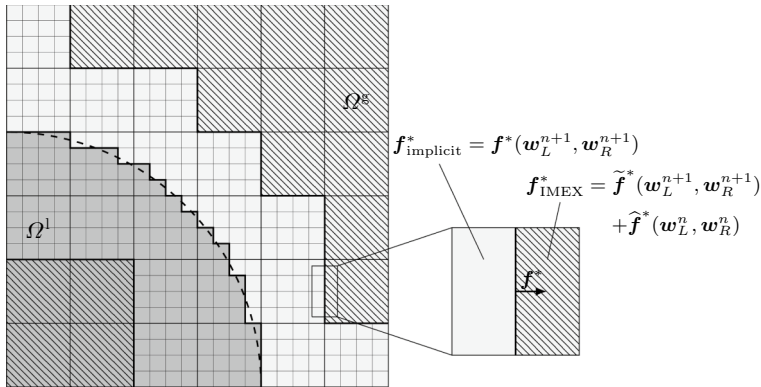


**Fig. 3** Schematic view of domain decomposition with the IMEX LSGFM. The zero isocontour of the level set is indicated with a dashed line. Hatched areas indicate the domain, where the TV splitting is applied. In the non-hatched domain, the Euler equations are treated fully implicitly. The fluxes at the interface of both domains is treated either fully implicitly (for the non-hatched domain) or partially implicitly and partially explicitly (for the hatched domain)

this work we do not use optimized scaling factors for the IMEX Runge-Kutta methods and simply choose the scaling factor 1. Therefore, the stability limit is not strictly  $CFL = 1$  but can be slightly below or above.

Additionally, a numerical flux function for the subsystems is required. We choose the standard TV flux proposed in [66] or the less dissipative TVHLL-LM Riemann solver which are given in Appendix A.

### 3.2.3 Spatial Discretization

With the TV flux splitting only the flux in the bulk phases can be split into an explicit and an implicit part. For the flux obtained by the two-phase Riemann solver ( $f_g^*$ ,  $f_l^*$ ), this is not possible for general two-phase Riemann solvers as physical modeling of two-phase effects is considered. This can include surface tension such as, e.g., in [20, 59] and phase transition, see, e.g., [22, 34]. Therefore, one can either treat this flux fully implicitly or fully explicitly. The latter would cause a timestep restriction depending on the acoustic waves and hence this flux is treated fully implicitly. Moreover, sub-cell elements that change their assignment from the liquid to the gaseous domain or vice versa cannot be treated partially implicit and partially explicit. Therefore, the cells located around the phase interface also have to be treated fully implicitly. This is realized with a narrow band of two elements adjacent to the interface in each direction, where no flux splitting is applied. This is illustrated in Fig. 3. Away from the interface, the TV splitting is used, indicated with the hatched area in Fig. 3. Inside the fully implicit narrow band, a finite volume sub-cell discretization is applied, whereas the DGSEM is used in the remaining IMEX flux splitting domain.

For the coupling of the IMEX flux splitting and the fully implicit domain, a special treatment is necessary. In analogy to domain-based IMEX methods, see, e.g., [38], the flux at the interface is calculated separately for both domains. That means that, during the flux calculation the neighboring domain is assumed to belong to the same type of the domain as the current element. With this, the numerical fluxes can be calculated as

$$\begin{aligned}
 f_{\text{IMEX}}^* &:= \tilde{f}^*(\mathbf{w}_L^{n+1}, \mathbf{w}_R^{n+1}, \mathbf{n}) + \hat{f}^*(\mathbf{w}_L^n, \mathbf{w}_R^n, \mathbf{n}), \\
 f_{\text{implicit}}^* &:= f^*(\mathbf{w}_L^{n+1}, \mathbf{w}_R^{n+1}, \mathbf{n}).
 \end{aligned}$$

With this approach conservativity at the coupling interface cannot be guaranteed. However, since the ghost fluid method is not conservative by construction, this influence is supposed to be small. In Sec. 4.3.2 this is experimentally justified (see Fig. 9 right).

Note that choosing the TV flux instead of the TVHLL-LM flux in the sub-cell directly neighboring the phase interface, has a favorable influence on the stability. Therefore, in those sub-cells always the TV flux is chosen as a Riemann solver. In the remaining domain one can either use the TV or the TVHLL-LM flux.

### 3.2.4 Temporal Discretization

In Fig. 2, the first order in time procedure has been shown. To increase the temporal accuracy, IMEX Runge-Kutta schemes [39] can be used for the advancement of the bulk phases and the level set field. Note that the coupling of both fields is still done only once per timestep and hence the global order of accuracy is not increased. Nevertheless, one can expect more accurate results by using higher order IMEX Runge-Kutta schemes.

In this work, globally stiffly accurate IMEX Runge-Kutta methods from [39] are used. The time integration procedure in semi-discrete form for a scheme with  $s$  stages, integrating from  $t^n$  to  $t^{n+1}$ , can be written as

- (i) for  $i = 1, \dots, s$ , solve for  $\mathbf{w}^{n,i}$

$$\mathbf{w}^{n,i} - \mathbf{w}^n + \Delta t \left( \sum_{j=1}^i \tilde{A}_{ij} \nabla_x \cdot \tilde{\mathbf{F}}(\mathbf{w}^{n,j}, t^n + \tilde{c}_j \Delta t) + \sum_{j=1}^{i-1} \hat{A}_{ij} \nabla_x \cdot \hat{\mathbf{F}}(\mathbf{w}^{n,j}, t^n + \hat{c}_j \Delta t) \right) = 0;$$

- (ii) set  $\mathbf{w}^{n+1} := \mathbf{w}^{n,s}$ .

The coefficients  $\tilde{A}_{ij}$ ,  $\hat{A}_{ij}$ ,  $\tilde{c}_j$  and  $\hat{c}_j$  are given in the Butcher table of the chosen method. Note that the second step only holds due to the globally stiffly accurate property of the chosen IMEX Runge-Kutta methods. The arising non-linear equation system

$$0 = \left( \mathbf{I} - \Delta t \tilde{A}_{i,i} \nabla_x \cdot \tilde{\mathbf{F}} \right) \mathbf{w}^{n,i} - \mathbf{b}^{n,i} =: \mathbf{g}(\mathbf{w}^{n,i}), \tag{8}$$

with  $\mathbf{b}^{n,i}$  denoting the sum of all values known from previous stages, is solved with a Jacobian-free Newton-GMRES method, see, e.g., [40] for an overview. Newton’s method for the solution of Eq. (8) requires an initial guess  $\mathbf{w}^0$  and a user defined tolerance  $\epsilon_{\text{Newton}}$  and is given by

- (i) for  $k = 0, 1, \dots$ , solve

$$\frac{d\mathbf{g}(\mathbf{w}^k)}{d\mathbf{w}^k} \Delta \mathbf{w}^k = -\mathbf{g}(\mathbf{w}^k), \mathbf{w}^{k+1} = \mathbf{w}^k + \Delta \mathbf{w}^k; \tag{9}$$

- (ii) set  $\mathbf{w}^{n,i} := \mathbf{w}^{k+1}$  when  $\|\mathbf{g}(\mathbf{w}^{k+1})\|_2 \leq \epsilon_{\text{Newton}} \|\mathbf{g}(\mathbf{w}^0)\|_2$ .

As initial guess, the solution at the previous stage is chosen, i.e.,  $\mathbf{w}^0 := \mathbf{w}^{n,i-1}$ . The linear system in Eq. (9) is then solved with a Jacobian-free GMRES method to ensure a small memory footprint. An analysis on the memory requirements of a matrix-free and a matrix-based approach for the DGSEM can be found in [68]. The arising Jacobian-vector product in the GMRES method is approximated via a first or a second order finite difference

$$\begin{cases} \frac{d\mathbf{g}(\mathbf{w}^k)}{d\mathbf{w}^k} \Delta\mathbf{w}^k \approx \frac{\mathbf{g}(\mathbf{w}^k + \Delta_{\text{FD}01} \Delta\mathbf{w}^k) - \mathbf{g}(\mathbf{w}^k)}{\Delta_{\text{FD}01}}, \\ \frac{d\mathbf{g}(\mathbf{w}^k)}{d\mathbf{w}^k} \Delta\mathbf{w}^k \approx \frac{\mathbf{g}(\mathbf{w}^k + \Delta_{\text{FD}02} \Delta\mathbf{w}^k) - \mathbf{g}(\mathbf{w}^k - \Delta_{\text{FD}02} \Delta\mathbf{w}^k)}{2\Delta_{\text{FD}02}}, \end{cases} \tag{10}$$

thus requiring one or two evaluations of the spatial operator per iteration of the linear solver. Note that  $\mathbf{g}(\mathbf{w}^k)$  can be stored and only has to be evaluated once per Newton iteration. The step sizes of the finite differences are chosen along the ideas from [1] and are given by

$$\Delta_{\text{FD}01} := \frac{\sqrt{\epsilon_{\text{machine}} \epsilon_{\text{scale}}^2}}{\|\Delta\mathbf{w}^k\|_2} \quad \text{and} \quad \Delta_{\text{FD}02} := \frac{\sqrt[3]{\frac{\epsilon_{\text{machine}}}{2} \epsilon_{\text{scale}}^2}}{\|\Delta\mathbf{w}^k\|_2}, \tag{11}$$

with the machine accuracy  $\epsilon_{\text{machine}}$  and the free parameter  $\epsilon_{\text{scale}}$ .

To accelerate the convergence of the GMRES method, a preconditioner is applied. As the purpose of the preconditioner is to approximate the Jacobian  $d\mathbf{g}(\mathbf{w})/d\mathbf{w}$  but being much simpler to invert, an elementwise block-Jacobi preconditioner is applied. It accounts for inner-element dependencies but neglects inter-element dependencies. Hence, it consists of one independently invertible matrix for each element. More details on the derivation of the block-Jacobi preconditioner for the mixed DG/FV sharp interface formulation can be found in [71].

*Timestep restriction* If no surface tension effects are considered, the timestep of the method is given by Eq. (7). Otherwise, the capillary timestep restriction [14] has to be considered as well. Taking this constraint additionally into account and following [14], the timestep is given by

$$\Delta t = \text{CFL} \cdot \min \left( \frac{l_{\text{ref}}}{|\hat{\lambda}|_{\max}(2N + 1)}, \frac{l_{\text{ref}}^*}{\lambda^\sigma} \right)_{\min_\Omega},$$

where the capillary eigenvalue  $\lambda^\sigma$  can be calculated as

$$\lambda^\sigma = \sqrt{\frac{2\pi\sigma}{\rho^* l_{\text{ref}}^*}} + |\mathbf{u}|^F$$

with the surface tension coefficient  $\sigma$  and the characteristic length of the FV sub-cells  $l_{\text{ref}}^* = l_{\text{ref}}/(N + 1)$ . Note that the capillary timestep constraint only has to be evaluated at FV sub-cell DOFs directly adjacent to the surrogate surface  $\Gamma$ . Differently to [14], we consider the total velocity of the flow at the interface  $|\mathbf{u}|^F$  and not only the velocity component tangential to the phase interface.

## 4 Validation and Efficiency of the IMEX LSGFM

In this section, the novel IMEX LSGFM is validated and the performance of the scheme is investigated. In particular, the separation of fast and slow waves and the semi-implicit interface coupling is validated and the efficiency gain compared to a fully explicit scheme is evaluated.

### 4.1 Validation of Domain Coupling

First, the correct coupling of the fully implicit and the IMEX domain is validated for one-dimensional settings.

*Acoustic wave interaction* The first setup is taken from [15] and describes a single acoustic pulse which interacts with a phase boundary of water and air. With this setup, inconsistencies in the discretization, especially in the coupling of the different parts of the domain, would show up as they can have a large influence on amplitudes and propagation speeds of the occurring waves. The velocity of the phase boundary itself is small, such that no discrete interface movement takes place.

At the left boundary of the domain  $\Omega = [0, 1.5 \text{ m}]$ , a small velocity pulse with the frequency  $f = 5000 \text{ s}^{-1}$  is prescribed by

$$u = \begin{cases} V_0 + \Delta u \sin\left(2\pi ft + \frac{3\pi}{2}\right), & \text{if } t < f^{-1}, \\ V_0 - \Delta u, & \text{else.} \end{cases}$$

The perturbation of the initial velocity  $V_0 = 1 \text{ m} \cdot \text{s}^{-1}$  is chosen as  $\Delta u = 0.02V_0$ . The remaining initial data are given by  $w_{\text{prim}}^0 = (1.157 \text{ kg} \cdot \text{m}^{-3}, V_0 - \Delta u, 10^5 \text{ Pa})^T$  for air and  $w_{\text{prim}}^0 = (998 \text{ kg} \cdot \text{m}^{-3}, V_0 - \Delta u, 10^5 \text{ Pa})^T$  for water. A Dirichlet boundary condition is prescribed on the right of the domain. On the left side of the domain air is presented with  $\gamma_{\text{air}} = 1.4$  and on the right side the water is modeled as a stiffened gas with  $\gamma_{\text{water}} = 4.1$  and  $p_\infty = 4.4 \times 10^8 \text{ Pa}$ . The interface is located at  $x_1 = 0.5 \text{ m}$ . With this initial data, the initial Mach number of the air is  $Ma \approx 2.8 \times 10^{-3}$ .

We discretize the domain with 175 elements with  $N = 5$ , couple them with the standard TV flux and choose the 3rd order IMEX-ARK3 scheme from [39] for the temporal discretization. As a comparison, the explicit scheme according to [37] with the explicit 3rd order low storage Runge-Kutta scheme from [69] is chosen.

According to [15], the ratio between the amplitude of the transmitted and the reflected acoustic wave is  $\Delta p_{\text{water}}^{\text{trans.}} / \Delta p_{\text{air}}^{\text{refl.}} = 2.001$ . We perform calculations with  $\text{CFL} = 1$  with respect to the acoustic eigenvalue and a simulation with the timestep increased by a factor of 100. The results of the simulations are depicted in Fig. 4.

If  $\text{CFL} = 1$  is chosen, a comparison with the explicit scheme is possible. One can hardly distinguish the two solutions (upper part of Fig. 4) and both have a similar ratio of the transmitted and reflected waves  $\Delta p_{\text{water}}^{\text{trans.}} / \Delta p_{\text{air}}^{\text{refl.}} = 2.016$ , which matches the analytical solution very well. Thus, our novel method reproduces the expected behavior and predicts the correct dynamics, if the associated waves are resolved sufficiently. For the increased timestep no calculations with the explicit scheme are possible and deviations from the afore observed dynamics are to be expected for the IMEX method (lower part of Fig. 4). One can see that due to the large timestep the dissipation and dispersion of the waves are increased. Nevertheless, the ratio of the waves still matches the analytical solution with  $\Delta p_{\text{water}}^{\text{trans.}} / \Delta p_{\text{air}}^{\text{refl.}} = 2.007$  with high accuracy.

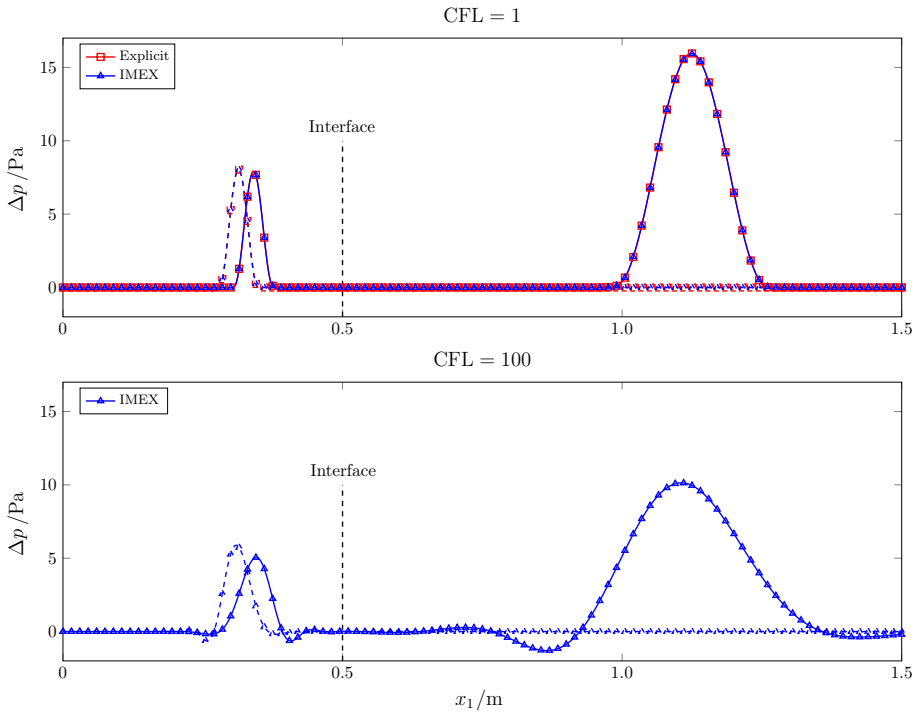


**Fig. 4** Pressure pulses before ( $t = 1$  ms, dashed) and after ( $t = 2$  ms, continuous) interaction with the phase interface at  $x_1 = 0.5$  m. Upper figure shows calculations with  $CFL = 1$  for explicit and IMEX scheme and lower figure with a 100 times larger timestep for the IMEX scheme

*Accelerated droplet* The next setup, taken from [3], describes the acceleration of a liquid due to a pressure difference in the surrounding gas. Differently to the previous setup, the phase interface moves and thus allows further validation of the IMEX LSGFM.

On the domain  $\Omega = [0, 1 \text{ m}]$  with Dirichlet boundary conditions, the initialization is given by  $w_{\text{prim}}^0 = (1 \text{ kg} \cdot \text{m}^{-3}, 0 \text{ m} \cdot \text{s}^{-1}, p^0)^T$  with

$$p^0 = \begin{cases} 2.5 \text{ Pa}, & \text{if } x_1 < 0.4 \text{ m}, \\ 1.0 \text{ Pa}, & \text{if } x_1 > 0.6 \text{ m}, \\ 1.75 \text{ Pa}, & \text{else.} \end{cases}$$

The gaseous phase ( $x_1 < 0.4 \text{ m}$  or  $x_1 > 0.6 \text{ m}$ ) is modeled as an ideal gas with  $\gamma_{\text{gas}} = 1.4$  and the liquid phase as a stiffened gas, using  $\gamma_{\text{liquid}} = 7.15$  and  $p_\infty = 3308 \text{ Pa}$ . The discretization is done with 100 elements with  $N = 3$ , TV flux and the 3rd order Runge-Kutta schemes from [39] and [69]. For the explicit scheme, the timestep is restricted with  $CFL = 1$ , whereas for the IMEX scheme the timestep is increased by a factor of 150. At the final time  $t_{\text{end}} = 0.065 \text{ s}$ , the maximum Mach number in the domain is  $Ma \approx 0.25$  and  $Ma \approx 2 \times 10^{-3}$  for the gaseous and the liquid phase, respectively.

The results of the computations are shown in Fig. 5. It is shown that the solutions in density and velocity are indistinguishable for the explicit and the IMEX scheme. Only for the pressure, differences are visible. While the explicit scheme predicts fast

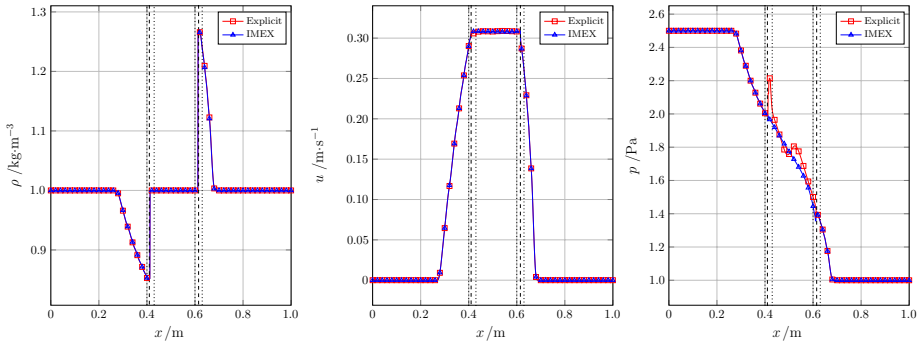


**Fig. 5** Density (left), velocity (middle) and pressure (right) distribution for accelerated one dimensional droplet at  $t_{\text{end}} = 0.065$  s for explicit and IMEX scheme. Dashed lines indicate the phase interface position and dotted lines indicate the interface between the fully implicit and the IMEX flux splitting domain

traveling waves inside of the droplet, the IMEX scheme predicts an almost linear pressure profile. This is to be expected as the IMEX scheme does not temporally resolve those waves, instead the linear pressure distribution of an incompressible material [3] is approximated.

### 4.2 Validation of Geometrical Coupling

Further validation of the novel scheme is provided by the simulation of the free droplet oscillation. This setup is particularly well suited for the validation of the consistent coupling of the different building blocks visualized in Fig. 2, as the whole dynamics is driven by the forces at the interface. Hence, a consistent coupling of interface properties, level set advection and the bulk phases is crucial.

The test setup describes an ellipsoidal shaped droplet at rest in a periodic domain  $\Omega = [-2 \text{ m}, 2 \text{ m}]^3$ . Due to surface tension, the droplet starts to oscillate. The initial data of the level set field is given by

$$\Phi^0(x) = \frac{x^2}{1.25^2} + \frac{y^2}{1^2} + \frac{z^2}{1^2} - 1,$$

and the remaining initial data are summarized in Fig. 6, with  $\sigma$  denoting the surface tension coefficient.

The choice of the material parameters ensures that the ratios of the speeds of sounds are similar to the ones given in [57] for water and air. For this setup the maximum occurring Mach numbers are  $Ma \approx 5 \times 10^{-3}$  and the analytical oscillation period for the  $l$ th mode can be calculated with the formula by Lamb [44]

$$T = \frac{2\pi \sqrt{r_{\text{equi}}^3 (\rho_{\text{air}} + (l + 1)\rho_{\text{water}})}}{\sqrt{\sigma(l - 1)l(l + 1)(l + 2)}},$$

**Fig. 6** Initial data of three dimensional test setup of oscillating droplet

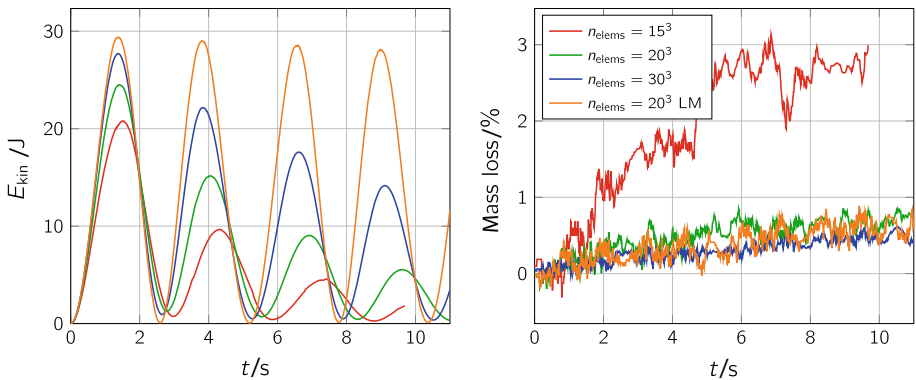
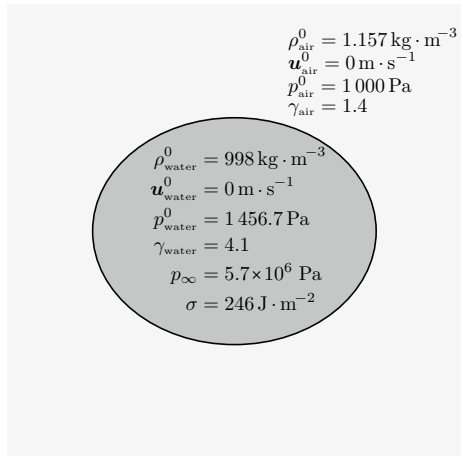


**Fig. 7** Temporal evolution of kinetic energy (left) and mass loss in percent (right) of surface tension-driven droplet oscillation, using different mesh resolutions. The simulation with the TVHLL-LM Riemann solver is indicated with “LM”

with the radius of the droplet in equilibrium  $r_{\text{equi}}$ . For the given initial data, the oscillation period of the second mode is  $T = 5$  s.

A grid convergence study is performed to validate the novel scheme. For that purpose, grids with  $15^3$ ,  $20^3$  and  $30^3$  elements with  $N = 3$  and TV or TVHLL-LM flux are used. The temporal discretization is done with the 4th order scheme IMEX-ARK4 from [39]. Instead of calculating the capillary timestep [14], the maximum timestep is prescribed with  $\Delta t_{\text{max}} = 10^{-3}$  s for the coarse meshes and  $\Delta t_{\text{max}} = 7 \times 10^{-4}$  s for the finest mesh.

Figure 7 shows the results in kinetic energy  $E_{\text{kin}} = \int_{\Omega} \frac{1}{2} \rho \|\mathbf{u}\|_2^2 d\Omega$  (left) and the mass loss (right). One can note that for a finer resolution the numerical viscosity is decreased and hence the damping of the oscillation is reduced, resulting in a smaller oscillation period. Considering the mass loss, also a convergent behavior can be observed, i.e., the mass loss decreases for a finer resolution. The figure shows that choosing the TVHLL-LM Riemann solver instead of the TV Riemann solver significantly improves the solution. While the mass loss is almost the same, much less numerical dissipation is introduced, resulting in a more accurate solution.



**Table 1** Oscillation period and its relative error (left) and relative mass loss for the surface tension-driven droplet oscillation with different mesh resolutions after one period: results with TV Riemann solver (upper) and TVHLL-LM Riemann solver (lower)

	Oscillation period $T/s$	Relative error/%	Mass loss/%
$n_{\text{elems}} = 15^3$ , TV	5.94	17.2	$\approx 2.6$
$n_{\text{elems}} = 20^3$ , TV	5.55	11.0	$\approx 0.5$
$n_{\text{elems}} = 30^3$ , TV	5.26	5.20	$\approx 0.3$
$n_{\text{elems}} = 20^3$ , TVHLL-LM	5.18	3.60	$\approx 0.4$

A quantitative analysis of the convergence study is provided in Table 1. One can see that the numerical solution approaches the analytical solution of  $T = 5$  s and the mass loss decreases under grid refinement.

Summing up, the presented studies validate the novel scheme. Investigations on the efficiency are provided in the next section.

### 4.3 Evaluation of the Efficiency

#### 4.3.1 Influence of the Approximation of the Jacobi-Vector Product

Choosing implicit time discretization opens the field of optimization of the (non-) linear solver parameters. One of the DOFs of the implicit method is the definition of the finite difference, approximating the Jacobian-vector product of the GMRES method, see Eq. (10). Here, one can choose a first or a second order finite difference and the step size of the finite difference (Eq. (11)). In literature, several options how to choose the step size can be found in Eq. (12)

$$\left\{ \begin{array}{ll} \epsilon_{\text{scale}}^{(1)} := p_{\text{air}}^0, & \epsilon_{\text{scale}}^{(2)} := \sqrt{1 + \|\mathbf{w}^k\|_2} \text{ [40]}, \\ \epsilon_{\text{scale}}^{(3)} := (\mathbf{w}^k)^T \cdot \Delta \mathbf{w}^k \text{ [12]}, & \epsilon_{\text{scale}}^{(4)} := \|\mathbf{w}^k\|_2 + \sqrt{\epsilon_{\text{machine}}} \|\Delta \mathbf{w}^k\|_2 \text{ [70]}, \\ \epsilon_{\text{scale}}^{(5)} := 1 + \frac{1}{n_{\text{DOF}}} \sum_i^{n_{\text{DOF}}} |\mathbf{w}_i^k| \text{ [40]}, & \epsilon_{\text{scale}}^{(6)} := \sqrt{n_{\text{DOF}}} \text{ [11]}, \end{array} \right. \quad (12)$$

with  $n_{\text{DOF}}$  denoting the total number of DOFs. For the present scheme, the simple choice  $\epsilon_{\text{scale}}^{(1)} := p_{\text{air}}^0$ , denoting the background pressure in the gaseous domain, is proposed. The choice of the scaling factor is a trade-off between truncation error of the finite difference and round-off errors due to limited machine accuracy.

A comparison between the different options is provided by the analysis of the required iterations for a certain amount of timesteps. For that purpose, the setup from the previous Sect. 4.2 with  $20^3$  elements,  $N = 3$  and TV flux is used. The amount of iterations are counted to advance the solution from  $t = 2$  s for 50 timesteps with IMEX-ARK4 and  $\Delta t = 10^{-3}$  s each. The relative convergence tolerance of Newton’s method is set to  $\epsilon_{\text{Newton}} = 10^{-4}$  and the relative convergence tolerance of the linear solver  $\epsilon_{\text{GMRES}}$  is varied. Two sets of simulations are executed: one with the parameters summarized in Fig. 6 and one with an increased background pressure of  $p_{\text{air}}^0 = 10^5$  Pa,  $p_{\text{water}}^0 = 1.004\,567 \times 10^5$  Pa and  $p_{\infty} = 5.7 \times 10^{-8}$  Pa, decreasing the occurring Mach numbers by a factor of 10. This allows an evaluation of the influence of the Mach number on the iterations. The results of the simulations are shown in Fig. 8.

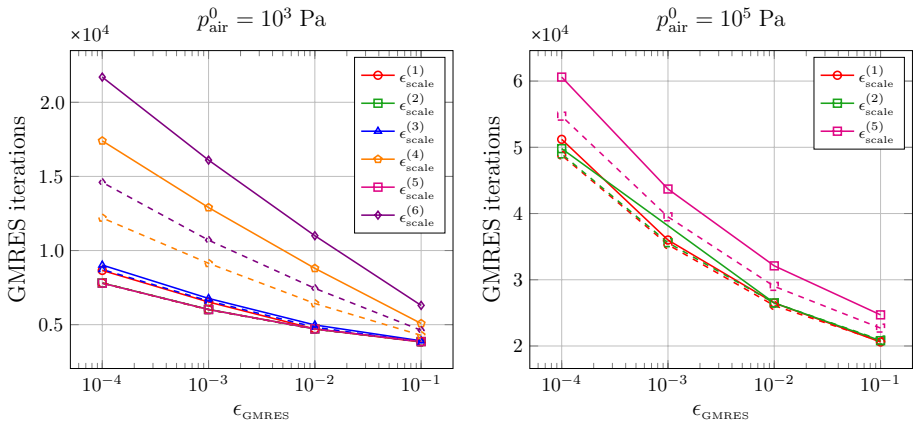


**Fig. 8** Required GMRES iterations to advance the surface tension-driven droplet from  $t = 2$  s for 50 timesteps with  $\Delta t = 10^{-3}$  s, using different convergence tolerances for the linear solver. Continuous lines indicate a first order finite difference and dashed lines indicate a second order finite difference for the approximation of the Jacobian-vector product

One can see that the choice of  $\epsilon_{\text{scale}}$  strongly influences the required amount of iterations. For the larger Mach number almost no differences between the different options are visible, except for the choices  $\epsilon_{\text{scale}}^{(4)}$  and  $\epsilon_{\text{scale}}^{(6)}$ , which require more iterations. In those two cases, the second order finite difference decreases the number of iterations. For the smaller Mach number, it is only possible to obtain a solution with  $\epsilon_{\text{scale}}^{(1),(2),(5)}$ . With the remaining options, convergence of the linear solver was not obtained with a maximum of 500 iterations per Newton step. From Fig. 8 one can conclude that with  $\epsilon_{\text{scale}}^{(1)}$  or  $\epsilon_{\text{scale}}^{(2)}$  a second order finite difference is not necessary for both considered setups. As the calculation of  $\epsilon_{\text{scale}}^{(1)}$  does not require any further computational effort, it is chosen for the following computations.

### 4.3.2 Comparison with Fully Explicit Scheme

Finally, a comparison with a fully explicit scheme regarding the required computational time is presented. With this comparison, the influence of the block-Jacobi preconditioner and the chosen timestep size on the computational resources is evaluated.

Again, the setup from Sec. 4.2 is taken with  $\epsilon_{\text{Newton}} = 10^{-3}$ ,  $\epsilon_{\text{GMRES}} = 10^{-1}$  and the CFL number is varied from  $\text{CFL} = 8 \times 10^{-4}$  to  $\text{CFL} = 8 \times 10^{-2}$ . Note that the CFL number is calculated with the maximum convective eigenvalue  $\hat{\lambda}_{\text{max}} = |\mathbf{u} \cdot \mathbf{n}|_{\text{max}}$ . The explicit reference scheme uses a 4th order low storage Runge-Kutta scheme from [6] for the time discretization with  $\text{CFL} = 0.9$  with respect to the acoustic eigenvalue. A comparison of the computational results is provided in Fig. 9.

It is clearly visible that the simulation results with the different CFL numbers and the explicit schemes are almost not distinguishable. Due to the similar solution quality those setups can be used to evaluate the influence of the timestep size on the required GMRES iterations and computational time.

For that purpose, five simulations from  $t = 1.99$  s to  $t = 2.04$  s are executed for each configuration on one node of the HPE “Hawk” system with 128 cores and the mean value is taken for the comparison. This choice leads to approximately 4 000 DOFs per core, what

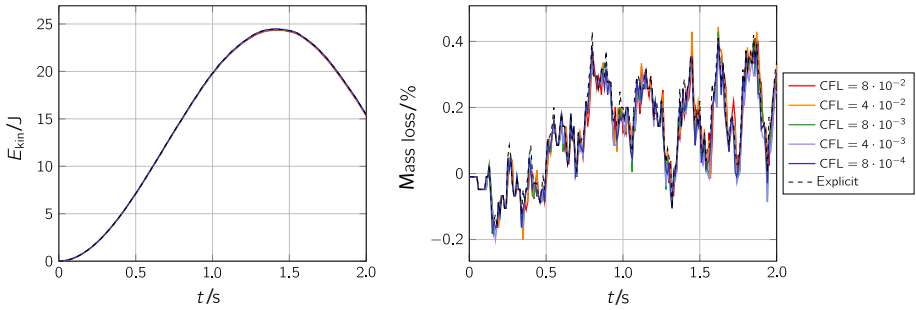


**Fig. 9** Kinetic energy (left) and relative mass loss (right) until  $t_{\text{end}} = 2\text{ s}$  for surface tension-driven droplet oscillation using different timestep sizes and explicit reference scheme. Solution of explicit scheme and IMEX scheme with different CFL numbers are almost not distinguishable

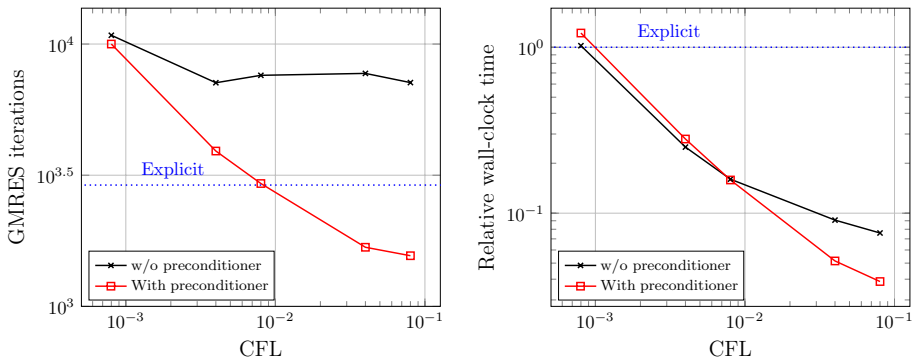


**Fig. 10** Required linear solver iterations (left) and relative computational time (right) to advance the surface tension-driven droplet oscillation from  $t = 1.99\text{ s}$  to  $t = 2.04\text{ s}$ . Wall-clock times are relative to the explicit reference scheme (marked with blue)

has turned out to be a good compromise between processor local work, communication and required memory.

First, the iterations of the linear solver are considered. Figure 10 (left) shows that the preconditioner has only a small influence on the convergence properties of the linear solver for small timesteps. For larger timesteps the block-Jacobi preconditioner allows to reduce the required amount of iterations significantly. While the required iterations are almost constant without preconditioner, the iterations are reduced for larger timesteps if the preconditioner is chosen. The amount of evaluations of the spatial operator for the explicit scheme is marked with blue. One can see, that with the IMEX scheme with large timesteps up to a factor of  $\approx 2$  less operator evaluations than with the explicit scheme are necessary.

Considering the required wall-clock time as a measure of efficiency shows that large speed-ups can be obtained using the novel IMEX scheme. Figure 10 (right) shows that a speed-up up to a factor of approximately 25 can be obtained compared to the explicit scheme. This large gain in wall-clock time is mainly due to the reduced amount of expensive operations that have to be executed in each timestep: velocity extrapolation, the evaluation of the interface geometry (i.e.,  $\mathbf{n}_\phi$  and  $\kappa_\phi$ ) are done once per timestep and the level set reinitialization is done only each second timestep. As those operations have a significant

influence on the overall computational time, large timesteps are a key feature to reduce the computational costs. Additionally, one can see that also here the use of the block-Jacobi preconditioner is beneficial for large timesteps. Although for small timesteps the computational time is increased due to the costs of building and applying the preconditioner, this is counterbalanced for large timesteps by the fewer iterations.

Concluding, the investigations in this section have shown that the novel IMEX LSGFM allows for an efficient and accurate simulation of low Mach number droplet dynamic phenomena. Compared to a fully explicit scheme, large gains in computational time can be achieved if large timesteps are chosen.

## 5 Application of the IMEX LSGFM

In this section, the novel scheme is applied to two more typical applications of low Mach number droplet dynamics to illustrate its capabilities.

### 5.1 Drop Impingement onto a Deep Pool

A typical field of low Mach number droplet dynamics is the impingement of droplets onto pools of various depth. In [58] a two dimensional numerical study on the influence of the Weber number, pool depth and impingement angle has been carried out. We utilize one specific setup of this study to illustrate and validate the capabilities of the IMEX LSGFM.

The impingement Weber number, defined as

$$We := \frac{2r\rho\|\mathbf{u}\|^2}{\sigma},$$

with radius  $r$ , density and velocity of the droplet of the simulation setup is  $We = 217$ . Gravity with the gravitation constant  $g = 9.81 \text{ m} \cdot \text{s}^{-2}$  is taken into account. The initial data and the boundary conditions of the computational domain are summarized in Fig. 11.

The domain  $\Omega = [-20r, 20r] \times [-5r, 15r]$  is discretized with  $400 \times 200$  elements with  $N = 2$ , which are coupled with the TVHLL-LM flux. The pool surface is located at  $x = 0 \text{ m}$  and has a depth of  $5r$  and the droplet center is initialized  $2r$  above the pool surface. With the parameters summarized in Fig. 11, an initial Mach number of approximately  $Ma = \|\mathbf{u}^0\|_{2,\text{drop}}/c_{\text{air}} = 1.7 \times 10^{-2}$  can be calculated. The characteristic momentum  $(\rho\mathbf{u})^* := \|\rho\mathbf{u}\|_2/\|(\rho^0\mathbf{u}^0)_{\text{water}}\|_2$  and the characteristic timescale  $\tau^* := 2r/\|\mathbf{u}^0\|_2$  are used to relate the occurring quantities to the initial conditions. The temporal discretization is done with the IMEX-ARK3 [39]. For stability reasons, the CFL number had to be reduced to  $\text{CFL} = 0.1$  for this example. Results of the simulation are shown in Fig. 12.

The figure shows that when the droplet hits the pool surface a jet is formed; in three dimensions named crown. Following, the crown height and the crater depth increase and a satellite droplet is ejected. This has also been observed in [58]. At  $t = 13.5\tau^* = 0.99 \text{ ms}$  the crater depth, the crown height and the angle of the crown are measured. A comparison with the results from [58], provided in Table 2, shows a good agreement. Deviations, especially in the crater depth and crown height are most likely due to the neglected viscous effects. Moreover, deviations caused by different numerical resolutions are possible as the number of DOFs is not reported in [58].

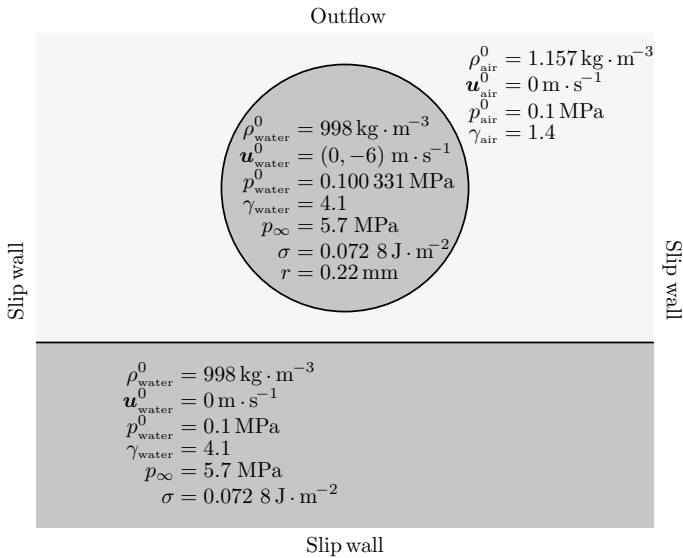


Fig. 11 Initial data of computational setup for drop impingement onto a deep pool

### 5.2 Binary Droplet Collision

A comparison with experimental data is possible for a three dimensional setup, where viscosity plays a minor role. This is the case for the binary head on collisions in [2] with a collision Weber number of  $We = 23$ . For this Weber number one can expect the coalescence of the droplets followed by a separation without ejecting further satellite droplets [2], see [63] for incompressible simulations of this setup. The initial data are summarized in Fig. 13. The domain  $\Omega = [0, 1 \text{ m}]^3$  is discretized with  $30^3$  elements with  $N = 2$  and describes one eighth of the total domain. At the boundaries, symmetry boundary conditions are prescribed and the TVHLL-LM flux is chosen as numerical flux function. With the parameters summarized in Fig. 13, an initial Mach number of  $Ma = \|\mathbf{u}^0\|_{2,\text{water}}/c_{\text{air}} = 5.7 \times 10^{-2}$  can be calculated. The temporal discretization is done with the IMEX-ARK3 scheme [39] and CFL = 0.9. The results of the simulation are reported in Fig. 14, together with the experimental results from [2]. One can see that the experimental results are reproduced with high accuracy: first the droplets merge and form a torus; due to the high surface tension they then elongate and finally separate again. All different type of shapes are correctly captured with the IMEX LSGFM.

### 6 Conclusion and Outlook

In this work it has been shown how an explicit LSGFM can be extended to deal with low Mach number flows. To increase the prohibitive small timestep of the explicit method, an IMEX flux splitting technique has been applied. It has been shown that by separating the domain into a fully implicit narrow band around the phase interface and into an IMEX flux splitting region, the timestep can be increased significantly. The separating of the domain became necessary as the interface flux and the narrow band region cannot be treated partially implicit and partially explicit.

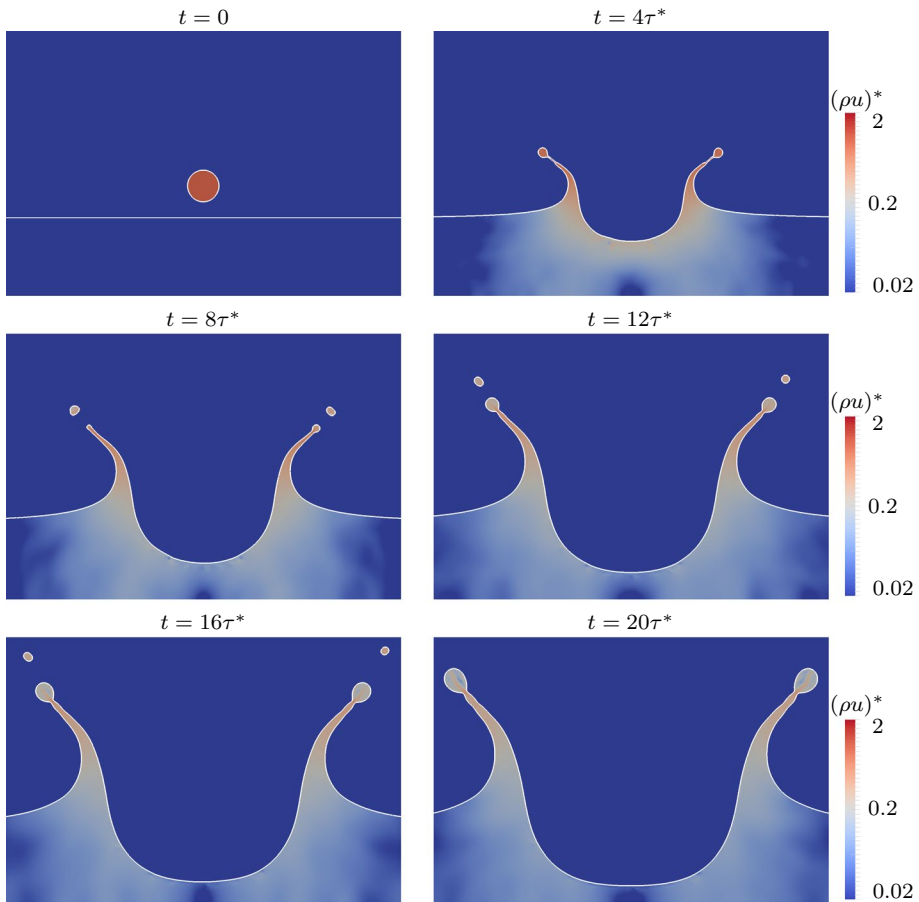


**Fig. 12** Snapshots of characteristic momentum of drop impingement onto a deep pool with the phase boundary being indicated with a white line

**Table 2** Comparison of drop impingement into a pool with depth  $5r$  and  $We = 217$  from [58] and with the IMEX LSGFM method

	Present simulation	Results from [58]
Crater depth	$\approx 3.5r$	$\approx 4.1r$
Crown height	$\approx 8.3r$	$\approx 9.0r$
Crown angle	$\approx 80^\circ$	$\approx 82^\circ$

A mixed discontinuous Galerkin/finite volume method has been used for the spatial discretization and IMEX Runge-Kutta schemes with a Jacobian-free Newton-GMRES method have been used for the temporal discretization.

The novel IMEX level set ghost fluid method has been validated and it has been shown that a large gain in computational time can be achieved compared to a fully explicit method. Applications to typical droplet dynamic problems illustrate the broad applicability of the developed scheme.

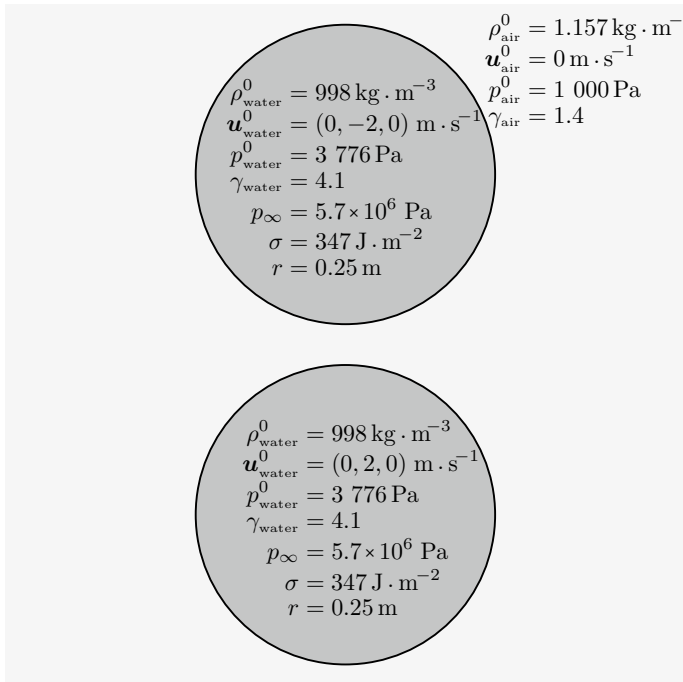


Fig. 13 Initial data of computational setup for binary droplet collision with  $We = 23$

A further improvement of the scheme is the consideration of viscous effects, i.e., choosing the Navier-Stokes equations over the Euler equations. This requires a consistent discretization of viscous effects at the phase boundary. Possible methods can, e.g., be based on the diffusive generalized Riemann problem [27, 28] or on the ideas in [43].

### Appendix A Riemann Solvers for the TV Splitting

*TV Riemann solver* For the sake of completeness, the standard TV flux from [66] is summarized here. The implicit numerical flux is given by

$$\tilde{\mathbf{f}}^*(\mathbf{w}_L, \mathbf{w}_R, \mathbf{n}) := \begin{pmatrix} 0 \\ p^* \mathbf{Id} \\ u^*(\rho^* \epsilon(\rho^*, p^*) + p^*) \end{pmatrix}_n,$$

and the explicit numerical flux is given by

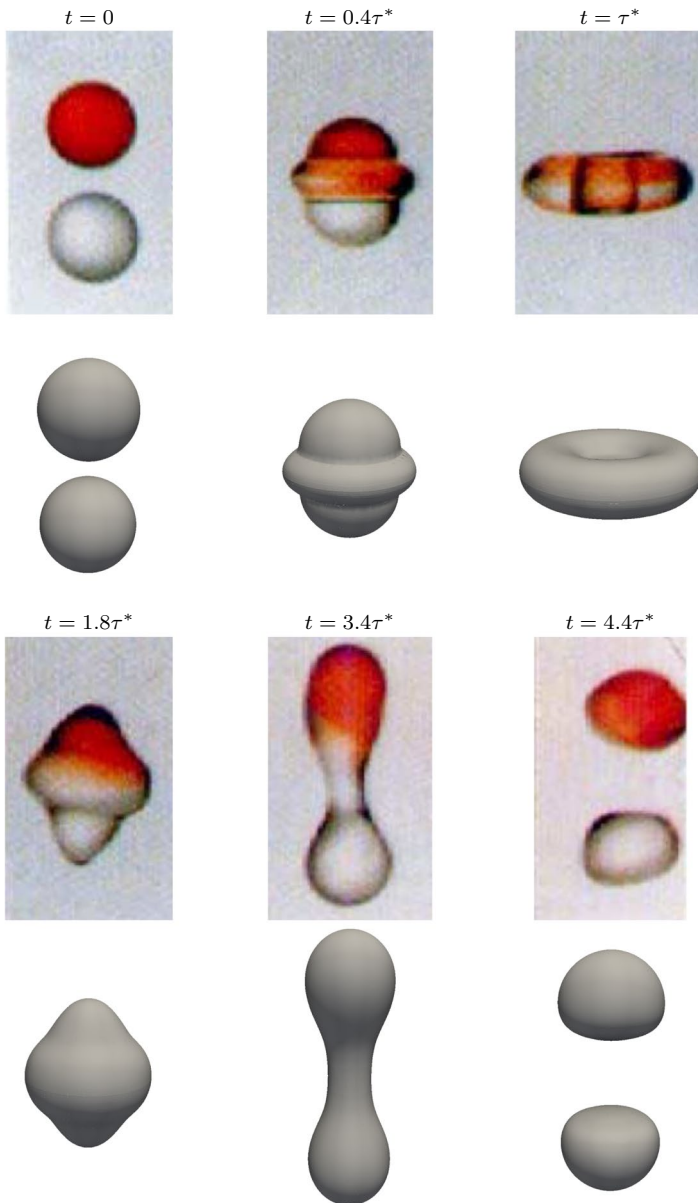


**Fig. 14** Temporal evolution of droplet surface for binary droplet collision with  $We = 23$ . Experimental results [2] (top) and current simulation (bottom)



$$\widehat{\mathbf{f}}^*(\mathbf{w}_L, \mathbf{w}_R, \mathbf{n}) := u^* \begin{cases} \begin{pmatrix} \rho \\ \rho \mathbf{u} \\ \frac{1}{2} \rho \|\mathbf{u}\|_2^2 \end{pmatrix}_{nL}, & \text{if } u^* \geq 0, \\ \begin{pmatrix} \rho \\ \rho \mathbf{u} \\ \frac{1}{2} \rho \|\mathbf{u}\|_2^2 \end{pmatrix}_{nR}, & \text{if } u^* < 0, \end{cases} \tag{13}$$

with the interface density, velocity and pressure

$$\begin{aligned} \rho^* &:= \begin{cases} \rho_L, & \text{if } u^* \geq 0, \\ \rho_R, & \text{if } u^* < 0, \end{cases} \\ u^* &:= \frac{C_R u_{1R} - C_L u_{1L}}{C_R - C_L} - \frac{2}{C_R - C_L} (p_R - p_L), \\ p^* &:= \frac{C_R p_L - C_L p_R}{C_R - C_L} + \frac{1}{2} \frac{C_R C_L}{C_R - C_L} (u_{1R} - u_{1L}), \end{aligned}$$

with

$$C_L := \rho_L(u_{1L} - A_L) \quad \text{and} \quad C_R := \rho_R(u_{1R} + A_R)$$

and  $A$  is given by Eq. (6). In the fully implicit region, the numerical flux is simply the sum of both parts

$$\mathbf{f}^*(\mathbf{w}_L, \mathbf{w}_R, \mathbf{n}) = \widetilde{\mathbf{f}}^*(\mathbf{w}_L, \mathbf{w}_R, \mathbf{n}) + \widehat{\mathbf{f}}^*(\mathbf{w}_L, \mathbf{w}_R, \mathbf{n}).$$

*TVHLL-LM Riemann solver* For small Mach numbers, the low dissipation TVHLL-LM solver can be used. A low dissipation numerical flux for low Mach numbers is obtained by modifying the HLL flux from [65] with the low Mach number fix according to [9]. For the explicit system the original flux of the TV flux is used, see Eq. (13). The implicit numerical flux is given by

$$\widetilde{\mathbf{f}}^*(\mathbf{w}_L, \mathbf{w}_R, \mathbf{n}) := \begin{cases} \widetilde{\mathbf{F}}_n(\mathbf{w}_L), & \text{if } S_L > 0, \\ \frac{1}{2} \left( \widetilde{\mathbf{F}}_n(\mathbf{w}_L) + \widetilde{\mathbf{F}}_n(\mathbf{w}_R) \right) \\ \quad - \frac{S_L + S_R}{S_R - S_L} \left( \widetilde{\mathbf{F}}_n(\mathbf{w}_L) + \widetilde{\mathbf{F}}_n(\mathbf{w}_R) \right) \\ \quad - \frac{2S_R S_L}{S_R - S_L} \left( \Delta \mathbf{w}_n^\rho + \min(1, M_{\text{loc}}) \Delta \mathbf{w}_n^u \right), & \text{if } S_L \leq 0 \leq S_R, \\ \widetilde{\mathbf{F}}_n(\mathbf{w}_R), & \text{if } S_R < 0. \end{cases}$$

The approximate wave speeds  $S_L$  and  $S_R$ , which are required for the HLL scheme can be calculated with

$$S_L := \min(S_{L1}, S_{L2}) \quad \text{and} \quad S_R := \max(S_{R1}, S_{R2}),$$

with the wave speed estimates

$$S_{L1} := \min(u_{1L} - c_L, u_{1R} - c_R)_n \quad \text{and} \quad S_{L2} := \frac{1}{2} \min(u_{1L} - A_L, u_{1R} - A_R)_n,$$

$$S_{R1} := \max(u_{1L} + c_L, u_{1R} + c_R)_n \quad \text{and} \quad S_{R2} := \frac{1}{2} \max(u_{1L} + A_L, u_{1R} + A_R)_n.$$

The jump terms  $\Delta w_n^u$  and  $\Delta w_n^p$  are given as

$$\Delta w_n^u := \frac{\rho_L + \rho_R}{2} \begin{pmatrix} 0 \\ \Delta u \\ \frac{1}{2} \Delta \|u\|_2^2 \end{pmatrix}_n \quad \text{and} \quad \Delta w_n^p := \Delta w_n - \Delta w_n^u,$$

with the jump  $\Delta(\cdot) = (\cdot)_L - (\cdot)_R$ . The low dissipation properties at low Mach numbers is ensured by multiplying  $\Delta w_n^u$  with a factor depending on the local Mach number

$$M_{\text{loc}} := \max \left( \left( \frac{\|u\|_2}{c} \right)_L, \left( \frac{\|u\|_2}{c} \right)_R, 10^{-4} \right).$$

**Acknowledgements** This paper contains some revised and extended results from the first author's PhD thesis work [71]. The authors kindly acknowledge the financial support provided by the Deutsche Forschungsgemeinschaft (DFG, German Research Foundation) through the project GRK 2160/1 "Droplet Interaction Technologies" and through the project no. 457811052. The simulations were performed on the national supercomputer HPE Hawk at the High Performance Computing Center Stuttgart (HLRS) under the *hpcdg* project.

**Funding** Open Access funding enabled and organized by Projekt DEAL.

## Compliance with Ethical Standards

**Conflicts of Interest** The authors declare that they have no conflict of interest.

**Open Access** This article is licensed under a Creative Commons Attribution 4.0 International License, which permits use, sharing, adaptation, distribution and reproduction in any medium or format, as long as you give appropriate credit to the original author(s) and the source, provide a link to the Creative Commons licence, and indicate if changes were made. The images or other third party material in this article are included in the article's Creative Commons licence, unless indicated otherwise in a credit line to the material. If material is not included in the article's Creative Commons licence and your intended use is not permitted by statutory regulation or exceeds the permitted use, you will need to obtain permission directly from the copyright holder. To view a copy of this licence, visit <http://creativecommons.org/licenses/by/4.0/>.

## References

1. An, H.B., Wen, J., Feng, T.: On finite difference approximation of a matrix-vector product in the Jacobian-free Newton-Krylov method. *J. Comput. Appl. Math.* **236**(6), 1399–1409 (2011)
2. Ashgriz, N., Poo, J.: Coalescence and separation in binary collisions of liquid drops. *J. Fluid Mech.* **221**, 183–204 (1990)
3. Boger, M., Jaegle, F., Klein, R., Munz, C.D.: Coupling of compressible and incompressible flow regions using the multiple pressure variables approach. *Math. Methods Appl. Sci.* **38**(3), 458–477 (2015)
4. Boger, M., Jaegle, F., Weigand, B., Munz, C.D.: A pressure-based treatment for the direct numerical simulation of compressible multi-phase flow using multiple pressure variables. *Comput. Fluids* **96**, 338–349 (2014)

5. Boscarino, S., Russo, G., Scandurra, L.: All Mach number second order semi-implicit scheme for the Euler equations of gasdynamics. *J. Sci. Comput.* **77**(2), 850–884 (2018)
6. Carpenter, M., Kennedy, C.: Fourth-order  $2N$ -storage Runge-Kutta schemes. Tech. rep, NASA Langley Research Center (1994)
7. Chalons, C., Coquel, F., Kokh, S., Spillane, N.: Large time-step numerical scheme for the seven-equation model of compressible two-phase flows. In: Först, J., Halama, J., Herbin, R., Hubert, F. (eds) *Finite Volumes for Complex Applications VI Problems & Perspectives*, Springer Proceedings in Mathematics, vol. 4, pp. 225–233. Springer, Berlin, Heidelberg (2011)
8. Chalons, C., Girardin, M., Kokh, S.: An all-regime Lagrange-projection like scheme for 2D homogeneous models for two-phase flows on unstructured meshes. *J. Comput. Phys.* **335**, 885–904 (2017)
9. Chen, S.S., Yan, C., Xiang, X.H.: Effective low-Mach number improvement for upwind schemes. *Comput. Math. Appl.* **75**(10), 3737–3755 (2018)
10. Chisholm, T.T., Zingg, D.W.: A Jacobian-free Newton-Krylov algorithm for compressible turbulent fluid flows. *J. Comput. Phys.* **228**(9), 3490–3507 (2009)
11. Choquet, R., Erhel, J.: Newton-GMRES algorithm applied to compressible flows. *Int. J. Numer. Methods Fluids* **23**(2), 177–190 (1996)
12. Cordier, F., Degond, P., Kumbaro, A.: An asymptotic-preserving all-speed scheme for the Euler and Navier-Stokes equations. *J. Comput. Phys.* **231**, 5685–5704 (2012)
13. Degond, P., Tang, M.: All speed scheme for the low Mach number limit of the isentropic Euler equation. *Commun. Comput. Phys.* **10**, 1–31 (2011)
14. Denner, F., van Wachem, B.G.: Numerical time-step restrictions as a result of capillary waves. *J. Comput. Phys.* **285**, 24–40 (2015)
15. Denner, F., Xiao, C.N., van Wachem, B.G.: Pressure-based algorithm for compressible interfacial flows with acoustically-conservative interface discretisation. *J. Comput. Phys.* **367**, 192–234 (2018)
16. Desjardins, O., Moureau, V., Pitsch, H.: An accurate conservative level set/ghost fluid method for simulating turbulent atomization. *J. Comput. Phys.* **227**(18), 8395–8416 (2008)
17. Du Chéné, A., Min, C., Gibou, F.: Second-order accurate computation of curvatures in a level set framework using novel high-order reinitialization schemes. *J. Sci. Comput.* **35**(2/3), 114–131 (2008)
18. Duret, B., Canu, R., Reveillon, J., Demoulin, F.: A pressure based method for vaporizing compressible two-phase flows with interface capturing approach. *Int. J. Multiph. Flow* **108**, 42–50 (2018)
19. Fechter, S.: Compressible multi-phase simulation at extreme conditions using a discontinuous Galerkin scheme. Ph.D. thesis, University of Stuttgart (2015)
20. Fechter, S., Jaegle, F., Schleper, V.: Exact and approximate Riemann solvers at phase boundaries. *Comput. Fluids* **75**, 112–126 (2013)
21. Fechter, S., Munz, C.D.: A discontinuous Galerkin-based sharp-interface method to simulate three-dimensional compressible two-phase flow. *Int. J. Numer. Methods Fluids* **78**(7), 413–435 (2015)
22. Fechter, S., Munz, C.D., Rohde, C., Zeiler, C.: Approximate Riemann solver for compressible liquid vapor flow with phase transition and surface tension. *Comput. Fluids* **169**, 169–185 (2018)
23. Fedkiw, R.P., Aslam, T., Merriman, B., Osher, S.: A non-oscillatory Eulerian approach to interfaces in multimaterial flows (the ghost fluid method). *J. Comput. Phys.* **152**(2), 457–492 (1999)
24. Föll, F., Hitz, T., Müller, C., Munz, C.D., Dumbser, M.: On the use of tabulated equations of state for multi-phase simulations in the homogeneous equilibrium limit. *Shock Waves* **29**(5), 769–793 (2019)
25. Frolow, R.: An efficient algorithm for the multicomponent compressible Navier-Stokes equations in low- and high-Mach number regimes. *Comput. Fluids* **178**, 15–40 (2019)
26. Fuster, D., Popinet, S.: An all-Mach method for the simulation of bubble dynamics problems in the presence of surface tension. *J. Comput. Phys.* **374**, 752–768 (2018)
27. Gassner, G., Lörcher, F., Munz, C.D.: A contribution to the construction of diffusion fluxes for finite volume and discontinuous Galerkin schemes. *J. Comput. Phys.* **224**(2), 1049–1063 (2007)
28. Gassner, G., Lörcher, F., Munz, C.D.: A discontinuous Galerkin scheme based on a space-time expansion II. Viscous flow equations in multi dimensions. *J. Sci. Comput.* **34**(3), 260–286 (2008)
29. Ghosh, D., Constantinescu, E.M.: Semi-implicit time integration of atmospheric flows with characteristic-based flux partitioning. *SIAM J. Sci. Comput.* **38**(3), A1848–A1875 (2016)
30. Haack, J., Jin, S., Liu, J.G.: An all-speed asymptotic-preserving method for the isentropic Euler and Navier-Stokes equations. *Commun. Comput. Phys.* **12**, 955–980 (2012)
31. Henneaux, D., Schrooyen, P., Dias, B., Turchi, A., Chatelain, P., Magin, T.: Extended discontinuous Galerkin method for solving gas-liquid compressible flows with phase transition. In: *AIAA Aviation Forum* (2020)

32. Hindenlang, F., Gassner, G., Altmann, C., Beck, A., Staudenmaier, M., Munz, C.D.: Explicit discontinuous Galerkin methods for unsteady problems. *Comput. Fluids* **61**, 86–93 (2012)
33. Hirt, C.W., Nichols, B.D.: Volume of fluid (VOF) method for the dynamics of free boundaries. *J. Comput. Phys.* **39**(1), 201–225 (1981)
34. Hitz, T.: On the Riemann problem and the Navier-Stokes-Korteweg model for compressible multiphase flows. Ph.D. thesis, University of Stuttgart (2019)
35. Huber, G., Tanguy, S., Béra, J.C., Gilles, B.: A time splitting projection scheme for compressible two-phase flows. Application to the interaction of bubbles with ultrasound waves. *J. Comput. Phys.* **302**, 439–468 (2015)
36. Jiang, G.S., Peng, D.: Weighted ENO schemes for Hamilton-Jacobi equations. *SIAM J. Sci. Comput.* **21**(6), 2126–2143 (2000)
37. Jöns, S., Müller, C., Zeifang, J., Munz, C.D.: Recent advances and complex applications of the compressible ghost-fluid method. In: SEMA SIMAI Springer Series, Proceedings of Numhpy 2019. Springer (2020). Accepted
38. Kanevsky, A., Carpenter, M.H., Gottlieb, D., Hesthaven, J.S.: Application of implicit-explicit high order Runge-Kutta methods to discontinuous-Galerkin schemes. *J. Comput. Phys.* **225**(2), 1753–1781 (2007)
39. Kennedy, C.A., Carpenter, M.H.: Additive Runge-Kutta schemes for convection-diffusion-reaction equations. *Appl. Numer. Math.* **44**, 139–181 (2003)
40. Knoll, D.A., Keyes, D.E.: Jacobian-free Newton-Krylov methods: a survey of approaches and applications. *J. Comput. Phys.* **193**, 357–397 (2004)
41. Kopriva, D.A.: Implementing Spectral Methods for Partial Differential Equations: Algorithms for Scientists and Engineers, 1st edn. Springer Publishing Company Incorporated, Springer, Dordrecht (2009)
42. Kraiss, N., Beck, A., Bolemann, T., Frank, H., Flad, D., Gassner, G., Hindenlang, F., Hoffmann, M., Kuhn, T., Sonntag, M., Munz, C.D.: FLEXI: a high order discontinuous Galerkin framework for hyperbolic-parabolic conservation laws. *Comput. Math. Appl.* **81**, 186–219 (2021)
43. Lalanne, B., Villegas, L.R., Tanguy, S., Risso, F.: On the computation of viscous terms for incompressible two-phase flows with level set/ghost fluid method. *J. Comput. Phys.* **301**, 289–307 (2015)
44. Lamb, H.: *Hydrodynamics*. Cambridge University Press, Cambridge (1932)
45. Lee, J., Son, G.: A level-set method for ultrasound-driven bubble motion with a phase change. *Numer. Heat Transf. Part A Appl.* **71**(9), 928–943 (2017)
46. Liu, W., Yuan, L., Shu, C.-W.: A conservative modification to the ghost fluid method for compressible multiphase flows. *Commun. Comput. Phys.* **10**(4), 785 (2011)
47. Main, A., Farhat, C.: A second-order time-accurate implicit finite volume method with exact two-phase Riemann problems for compressible multi-phase fluid and fluid-structure problems. *J. Comput. Phys.* **258**, 613–633 (2014)
48. Marchandise, E., Geuzaine, P., Chevaugneon, N., Remacle, J.F.: A stabilized finite element method using a discontinuous level set approach for the computation of bubble dynamics. *J. Comput. Phys.* **225**(1), 949–974 (2007)
49. Merkle, C., Rohde, C.: The sharp-interface approach for fluids with phase change: Riemann problems and ghost fluid techniques. *ESAIM Math. Model. Numer. Anal.* **41**(6), 1089–1123 (2007)
50. Müller, C., Hitz, T., Jöns, S., Zeifang, J., Chiocchetti, S., Munz, C.D.: Improvement of the level-set ghost-fluid method for the compressible Euler equations. In: Lamanna, G., Tonini, S., Cossali, G.E., Weigand, B. (eds) *Droplet Interaction and Spray Processes*. Springer, Heidelberg (2020)
51. Noelle, S., Bispfen, G., Arun, K.R., Lukáčová-Medvid'ová, M., Munz, C.D.: A weakly asymptotic preserving low Mach number scheme for the Euler equations of gas dynamics. *SIAM J. Sci. Comput.* **36**, B989–B1024 (2014)
52. Olsson, E., Kreiss, G.: A conservative level set method for two phase flow. *J. Comput. Phys.* **210**(1), 225–246 (2005)
53. Olsson, E., Kreiss, G., Zahedi, S.: A conservative level set method for two phase flow II. *J. Comput. Phys.* **225**(1), 785–807 (2007)
54. Osher, S., Sethian, J.A.: Fronts propagating with curvature-dependent speed: algorithms based on Hamilton-Jacobi formulations. *J. Comput. Phys.* **79**(1), 12–49 (1988)
55. Peluchon, S., Gallice, G., Mieussens, L.: A robust implicit-explicit acoustic-transport splitting scheme for two-phase flows. *J. Comput. Phys.* **339**, 328–355 (2017)
56. Peng, D., Merriman, B., Osher, S., Zhao, H., Kang, M.: A PDE-based fast local level set method. *J. Comput. Phys.* **155**(2), 410–438 (1999)
57. Perigaud, G., Saurel, R.: A compressible flow model with capillary effects. *J. Comput. Phys.* **209**(1), 139–178 (2005)

58. Ray, B., Biswas, G., Sharma, A.: Oblique drop impact on deep and shallow liquid. *Commun. Comput. Phys.* **11**(4), 1386–1396 (2012)
59. Schleper, V.: A HLL-type Riemann solver for two-phase flow with surface forces and phase transitions. *Appl. Numer. Math.* **108**, 256–270 (2016)
60. Sonntag, M., Munz, C.D.: Shock capturing for discontinuous Galerkin methods using finite volume subcells. In: Fuhrmann, J., Mario, O., Christian, R. (eds) *Finite Volumes for Complex Applications VII-Elliptic, Parabolic and Hyperbolic Problems*, pp. 945–953. Springer (2014)
61. Sonntag, M., Munz, C.D.: Efficient parallelization of a shock capturing for discontinuous Galerkin methods using finite volume sub-cells. *J. Sci. Comput.* **70**(3), 1262–1289 (2017)
62. Sussman, M., Smereka, P., Osher, S.: A level set approach for computing solutions to incompressible two-phase flow. *J. Comput. Phys.* **114**(1), 146–159 (1994)
63. Tanguy, S., Berlemont, A.: Application of a level set method for simulation of droplet collisions. *Int. J. Multiph. Flow* **31**(9), 1015–1035 (2005)
64. Tavelli, M., Dumbser, M.: A pressure-based semi-implicit space-time discontinuous Galerkin method on staggered unstructured meshes for the solution of the compressible Navier-Stokes equations at all Mach numbers. *J. Comput. Phys.* **341**, 341–376 (2017)
65. Tiam Kapen, P., Ghislain, T.: A new flux splitting scheme based on Toro-Vazquez and HLL schemes for the Euler equations. *J. Comput. Methods Phys.* **2014**, 827034 (2014)
66. Toro, E.F., Castro, C.E., Lee, B.J.: A novel numerical flux for the 3D Euler equations with general equation of state. *J. Comput. Phys.* **303**, 80–94 (2015)
67. Toro, E.F., Vázquez-Cendón, M.E.: Flux splitting schemes for the Euler equations. *Comput. Fluids* **70**, 1–12 (2012)
68. Vangelatos, S.: On the efficiency of implicit discontinuous Galerkin spectral element methods for the unsteady compressible Navier-Stokes equations. Ph.D. thesis, University of Stuttgart (2019)
69. Williamson, J.H.: Low-storage Runge-Kutta schemes. *J. Comput. Phys.* **35**, 48–56 (1980)
70. Woodward, C.S., Gardner, D.J., Evans, K.J.: On the use of finite difference matrix-vector products in Newton-Krylov solvers for implicit climate dynamics with spectral elements. *Proc. Comput. Sci.* **51**, 2036–2045 (2015)
71. Zeifang, J.: A discontinuous Galerkin method for droplet dynamics in weakly compressible flows. Ph.D. thesis, University of Stuttgart (2020)
72. Zeifang, J., Kaiser, K., Beck, A., Schütz, J., Munz, C.D.: Efficient high-order discontinuous Galerkin computations of low Mach number flows. *Commun. Appl. Math. Comput. Sci.* **13**(2), 243–270 (2018)
73. Zeifang, J., Kaiser, K., Schütz, J., Massa, F.C., Beck, A.: An investigation of different splitting techniques for the isentropic Euler equations. In: Lamanna, G., Tonini, S., Cossali, G.E., Weigand, B. (eds) *Droplet Interaction and Spray Processes. Fluid Mechanics and Its Applications*, vol. 121, pp. 45–55. Springer, Heidelberg (2020)
74. Zeifang, J., Schütz, J., Kaiser, K., Beck, A., Lukáčová-Medvid'ová, M., Noelle, S.: A novel full-Euler low Mach number IMEX splitting. *Commun. Comput. Phys.* **27**, 292–320 (2020)